This article has been published in: Injury. 2018 Sep;49 Suppl 2:S11-S21.

BIOCHEMICAL ASSESSMENT OF NANOSTRUCTURES IN HUMAN TRABECULAR BONE: PROPOSAL OF A RAMAN MICROSPECTROSCOPY BASED MEASUREMENTS PROTOCOL

Short title: Raman analysis of trabecular bone.

Authors: Manuel Toledano[1], Manuel Toledano-Osorio[1], Enrique Guerado[2], Enrique Caso[3], Fátima S. Aguilera[1*], Raquel Osorio[1].

Institution: [1]University of Granada, Faculty of Dentistry, Dental Materials Section.

[2]Department of Orthopaedic Surgery and Traumatology. Hospital Universitario Costa del Sol. University of Malaga. Marbella. Malaga. Spain.

[3]Research Unit. Hospital Universitario Costa del Sol. University of Malaga. Marbella. Malaga. Spain.

Address: [1]University of Granada, Faculty of Dentistry, Dental Materials Section. Colegio Máximo de Cartuja s/n 18071 Granada. Spain.

[2,3] Hospital Universitario Costa del Sol. University of Malaga. Dual carriageway Km 187, 29603 Marbella. Malaga. Spain

*Corresponding author: Prof. Fátima S. Aguilera
University of Granada, Faculty of Dentistry
Dental Materials Section
Colegio Máximo de Cartuja s/n
18071 – Granada - Spain.
Tel.: +34 958243793
Email: fatimas@ugr.es

Abstract

Background: Improvements to the understating of the compositional contributions of bone mineral and organic components to the competence of trabecular bone are crucial. The purpose of this study was to propose a protocol to study biochemical composition of trabecular bone, based on two combined Raman analysis methodologies.

Material and Methods: Both cluster and single point Raman mappings were obtained, in order to assess bone degeneration associated with aging, disease, or injury, and to help in the evaluation and development of successful therapies. In this study, human trabecular bone has been analysed throughout a) Raman cluster analysis: bone mineral content, carbonate-to-phosphate ratio (both from the mineral components), the crosslinking and nature/secondary structure of collagen (both from the organic components); and b) Single point Raman spectra, where Raman points related to the minerals and organic components were also obtained, both techniques were employed in spectra attained at 400 to 1700 cm^{-1}.

Results: Multivariate analysis confirmed: 1) the different spectral composition, 2) the existence of centroids grouped by chemical affinity of the various components of the trabecular bone, and 3) the several traces of centroids and distribution of chemical compositional clusters.

Conclusions: This study is important, because it delivers a study protocol that provides molecular variations information in both mineral and collagen structure of trabecular bone tissue. This will enable clinicians to benefit knowing the microstructural differences in the bone subjected to degeneration of their patients.

Key words: Raman, trabecular bone, chemical, analysis.

Introduction

From a pure biomaterial perspective, bone can be considered as a hydroxyapatite solid reinforced by a collagen network[1]. There are generally two types of bone tissue, trabecular and cortical. Trabecular bone is a highly porous structure that fills the proximal and distal ends of all bones (*e.g*, femur) and is also present as a filler in other bones (e.g. vertebral bodies and both maxillar bones), providing structural support and flexibility[2].

The vast majority of the research work has been focused on the histological, microscopic and mechanical aspects of bone, but rarely on the underlying molecular structure which is integral to a full understanding of the disease, especially its effect on the mineral content and collagen matrix[3]. Raman spectroscopy is a vibrational spectroscopy technique used to assess scattered light from biologic molecules and ions. Raman scattering occurs when molecules within a specimen are excited by incident laser light. Vibrational motions within the molecules lead to a small fraction of the light (approximately one in 10^7 photons) losing energy and being scattered at longer wavelengths. The wavelength difference between scattered and incidence light corresponds to molecular vibrations and leads to bands at characteristics frequency shifts in the Raman spectrum. These shifts are labeled in wavenumber units corresponding to the vibrational energy (cm^{-1})[4]. Raman spectroscopy, considered as an analytical and nondestructive technique is able to measure the molecular composition by providing a spectrum that contains information regarding all the chemical bonds present within the sample[5]. Bone Raman spectra contains molecular composition information that is related to risk of fracture[4]. The strength of Raman spectroscopy as a bone quality measurement tool should be emphasised.

Micro-Raman mapping with cluster analysis provides a direct insight on biochemical nature, molecular structure and scattering techniques, as spectroscopies of tissue. It is used as a quantitative chemical assessment methodology for biological samples in conjunction with the fact that the Raman peak intensity is proportional to the number of molecules within the volume of the scanned area[6]. It is a sensitive method capable of identifying individual spectral bands arising from the inorganic calcium phosphate crystals and the protein/lipid constituents of hard tissues[7]. Clustering is a multivariate technique for statistical data analysis similar to image analysis and pattern recognition. It finds intrinsic clusters from the region of interest spectra without using any additional a-priori information [classical least-squared (CLS)] about the samples. Clustering applied on the raw spectra mainly distinguishes the concentration of constituents, while derivation of the spectra prior to clustering leads to differentiation by the structural differences. Raman spectroscopy, in combination with multivariate data analysis, is a label free imaging method for the analysis of trabecular bone sections. This combined approach yields images depicting a semi-quantitative distribution of the biochemical species in the tissue with high resolution[8]. Various methods of multivariate analysis[9,10], like principal component analysis (PCA), clustering k-means (KMC), and hierarchical cluster algorithm (HCA) produces a complete hierarchy of different clusters[11] for analysing Raman two dimensional *data*. Compared to the conventional histological and microscopic methods Raman spectroscopy and cluster analysis result advantageous because they are fast, non-intrusive, stain-free, quantitative and less prone to subjectivity. The combination of various chemometric methods is essential in providing different images conveying complementary information about the tissue, for studying biochemical and morphological changes during bone degradation and remineralisation.

Single point Raman spectra, permits to image a line profile thorough a series of point-to-point sampling. The spectroscopic images, as functions of Raman intensity and special coordinates, allow an assessment of the chemical heterogeneity of a specimen in terms of the spatial distribution of the system's molecular constituents[12]. Thus, the Raman peak intensity is proportional to the number of molecules within the volume of the scanned area[6]. Hence, the total acquisition time equals the number of sample position observed, plus any overhead associated with sample motion. At first glance, line imaging appears quite similar, with an end result of a data set consisting of intensity *vs* Raman shift and position along a line[13]. It furnishes biochemical specificity because it is based on spectral peaks specific to the biochemical and structural properties of bone mineralisation[14,15,16]. Point Raman mapping, as example of serial (raster) imaging approaches, involves a laser spot sample illumination. In point mapping, a laser spot is stepped, or raster scanned, in two spatial dimensions (x and y) with a spectrum being recorded at each x,y position[12]. This technique is sufficiently sensitive to differences in mineral and organic compositions that can be used to identify damaged, damage-susceptible or restored bone areas, and possibly explain why certain regions of bone are subject to fracture. The main advantages of Raman spectroscopy include its application to fresh tissue and a high spatial resolution, with sampling volumes of 1 μm^3 or less[4]. Combining the two technologies, *i.e*, cluster and single point Raman spectra, takes advantage of their synergies for characterizing lesions and for providing objective biochemical information at ultrastructural levels[4].

Although several authors have discussed the advantages of the various Raman imaging methodologies, the studies generally emphasized only theoretically achievable signal-to-noise ratios, rather than presenting comparable experimental data. The objective of the present study was to propose a study protocol for trabecular bone, based on two combined

Raman analysis methodologies, cluster and single point Raman mapping, in order to assess the existence of degenerative bone diseases and to help with the evaluation and development of successful therapies.

Materials and Methods

Femoral neck biopsy specimens

Study subjects were hip fractured postmenopausal women undergoing surgery for total hip replacement, and the specimens were retrieved from the base of the femoral neck. Subjects consented to undergo a femoral neck biopsy. All protocols were approved by the Institutional Review Board, prior to obtain biopsy samples. These samples were then kept immersed in a phosphate -buffered saline (PBS) solution (pH 7.4) and stored frozen at -20ºC[17]. The biopsy specimens were processed in epoxy resin[18]. To prepare the specimens for Raman analysis, the epoxy-resin-embedded biopsy specimens that were used to generate sections, were further polished with different diamond pastes, from 10 μm to 0.1 μm in diameter, to obtain smooth surfaces. Measurements were performed on randomly selected femoral specimens and ~4-5 different trabeculae were tested from each sample[19,20].

Raman spectroscopy and clusters analysis

A dispersive Raman spectrometer/microscope (Horiba Scientific Xplora, Villeneuve d´Ascq, France) was used to analyse the previous section of epoxy resin-embedded bone. A near-infrared diode laser spot size of ≈ 0.5μm^2, operating at 785 nm, was used to measure the Raman signal (100 mW power at sample surface) from 400 to 1700 cm^{-1} Raman wave number. A X100/0.90 NA air objective was employed to focus the laser on the sample and collect the Raman signal. The spectrometer was equipped with a CCD

detector (DR-324B-FI-327, Andor Technology LTD, UK). Raman signal was acquired using a 600-lines/mm grating. Calibration of the wavelength and intensity was performed according to manufacturer's specification using a silicon standard and calibration system integrated with the LabSpec 6.3 Analysis software. In order to ascertain that measured intensities are meaningful, all measurements were performed under the same laser excitation power and the same measurements conditions. For microspectroscopy, the confocal hole size was set at 300μm and the slit size at 100 μm. The spectral resolution of the system was 6.25cm^{-1}. Shown mapping spectra correspond to the mean of a total of 50 individual Raman taken over a 10 x 10 μm surface of the sample, with a 2.5 μm point interval. Each spectrum was measured by using 10 s acquisition time with 5 accumulations. The mineral and organic components of bone were examined through cluster analysis. For hierarchical cluster algorithm (HCA) Raman imaging, each dataset was assessed to automatically distinguish regions of the scanned area with different Raman features[21]. For each specimen, a 10μm x 10μm area of the surface was mapped using 1 μm spacing at X and Y axes, at 100x magnification. A total of 144 points were performed per map. In the cluster analysis routine, PCA scores were taken as input variables, squared Euclidean distances were used as distances measures, and Ward's algorithm was used to partition Raman spectra into cluster. PCA decomposed data set into a bilinear model of linear independent variables, the so-called principal components (PCs). It was hence used for identifying significant spectral differences among distinct substrata. Clusters were created following Ward's technique and the dendrogram was calculated applying three factor spectra or principal components, corresponding to three different histological locations of trabecular bone. The number of clusters, three, were chosen according to several issues, such as the dendrogram structure, the false-color maps and the cluster centroid[8]. Once clusters were formed (HCA images), average spectra

(centroids) (HCA results) were calculated for each cluster. It resulted in the calculation of a new coordinate system whereby variations of the dataset is described via new axes, principal components (PCs) and classical least-square (CLS) fitting analysis. Thus, CLS analysis of data sets can be performed quickly and simply to provide information on peak parameters (*e.g.*, position, width, amplitude, area) and component contribution in Raman images. The CLS protocol was operated within the LabSpec 6 spectroscopy software suite (Horiba Scientific Xplora, Villeneuve d´Ascq, France) with the multivariate images analyser. At this point, the mineral and organic component of bone, were analysed as follows:

Bone mineral content (BMC):

1. *Phosphate* (960 cm^{-1}) *and carbonate* (1070 cm^{-1}) *peaks and areas of their bands.* Peak heights were processed in absorbance units. The carbonate band may be partially overlapped by another phosphate band around 1076 cm^{-1}, reducing the measurement precision, especially for apatites with minimal carbonate content[4].
2. *Mineral-to-matrix ratio (mineralisation) (MMR)*: It was inferred from the visible ratio of the intensities of the peaks at 958 cm^{-1} (phosphate v_1) (PO_4^{3-}) to methylene side chains at 1447 cm^{-1} (CH_2)[22,23], in order to quantitatively calculate the extent of mineralisation. This ratio is the strongest predictor of mechanical properties[4]. A decrease in the mineral-to-matrix ratio may also be attributed to changes in hormone levels, which have been known to regulate bone remodeling[4]. At fracture boundaries, irregular pattern of mineral loss, *e.g*, mineral-to-matrix ratio are observed[24]. Other carbonate -to-amide I (at 1665 cm^{-1}) ratios, may indicate bone remodeling[4].

Crystallinity: It was evaluated based on the full width at half maximum (FWHM) of the phosphate band at 960 cm^{-1}. This index expressed the crystallographic or relative atomic order, since a narrow peak suggest less structural variation in bond distances and angles[25]. In general, the narrowest the spectral peak width is, the highst the degree of mineral crystallinity[26]. Crystallinity, also correlated with both mineral-to-matrix ratio and carbonate-to-phosphate, has been related to modulus, yield stress, and fracture stress[4,23].

Carbonate-to-phosphate ratio (carbonate substitution): It was assessed as the ratio of the type-B carbonate at 1070 cm^{-1} to phosphate v_1[23]. Mineral crystallinity, the mineral phosphate band at 960 cm^{-1} and carbonate band at 1070 cm^{-1} increase with tissue age[4].

The organic component of bone was analysed examining the following parameters:

Normalisation: Phenyl group: The peak at 1003 cm^{-1}, which is assigned to C-C bond in the phenyl group, was used for normalisation[27].

Crosslinking:

1. Pyridinium ring vibration: In the spectra, the peak appeared at 1030/1032.7 cm^{-1}, is assigned to the C-C in pyridinium ring vibration which has a trivalent amino acid crosslinking residue[28]. The relative intensity of this peak increases after the crosslinking formation[29].
2. AGEs (advance glycation end products)-pentosidine at 1550 cm^{-1}, interpreted as a marker of the aging process[30].

Nature and secondary structure of collagen:

1. Amide III, CH_2 and Amide I: The peaks at 1246/1270, 1454-1461 and 1626/1656 cm^{-1}, assigned to amide III, CH_2 and amide I, respectively, are sensitive to the molecular conformation of the polypeptide chains[27,29,31]. The decrease of amide I peak indicates damage or removal of collagen fibrils[32]. A shift in the bone matrix amide I band position may be indicative of ruptured collagen crosslinks, altered

collagen quality induced by aging, hydration/dehydration or radiologic damage[33,34]. At fracture boundaries, a collagen quality parameter reduction is observed[35].

2. Ratio amide I/amide III concerned the organisation of collagen[36].
3. Ratio amide I/AGEs-Pentosidine, indicatives of the glycation reaction *vs* collagen scaffolding[36].
4. Ratio amide I/CH_2 indicates altered collagen quality[36].
5. The peak at 1340 cm^{-1} has been assigned to protein α-helices, where its intensity is sensitive to molecular orientation[7].

Single point Raman spectra analysis

The experimental conditions were similar to the cluster analysis, except that the Raman wavenumber ranged from 200 to 2000 cm^{-1}, and that the spectral images corresponded to selected areas of a 25 x 7.5 µm surface of the sample, with a 2.5 µm point interval. Baseline correction was always performed after acquisition in order to subtract background, a 5^{th} degree polynomial function was used for that purpose. At this point, the Raman spectroscopic peaks of both mineral and organic components found in the trabecular bone were assessed.

Mineral components:

1. Bands assigned to vibrations of carbonated calcium phosphate in an apatitic lattice are 430 and 451 cm^{-1} (v_2 mode) [37].
2. Symmetric bending mode (v_2) PO_4^{3-}, at 431 and 446 cm^{-1} peaks. These two bands are present in sound and demineralised substrata. In demineralised spectra, 431 cm^{-1} peak intensity is greater than 446 cm^{-1} peak[14].

3. Changes in fluoridated apatite (575 cm^{-1}) reflect bacterial metabolic activity and organic content[38].
4. Peaks at 579, 590, 608, 614 cm^{-1} (v_4 asymmetric bending mode PO_4^{3-}). Band pair 579, 590 shows greater intensity in the demineralised spectrum but weaker intensity in the sound spectrum[14].
5. 960 cm^{-1} is linked with nonaromatic mode v_1 PO_4^{3-} [39].
6. The microdamaged and fractured regions showed a higher wavenumber at 963 cm^{-1} and 965 cm^{-1} [40].
7. Strong monohydrogen phosphate v_1 vibration (~1003 cm^{-1}) indicates areas where active remodeling are occurring, performing as a probe of mineral structure and substitution, in junction with the phosphate v_1 vibration (~960 cm^{-1})[37].
8. The intensity ratio plot shows enhanced 431/960, 446/960, 579/960, 590/960, 1043/960, 1069/960 at the demineralised lesion[14].
9. The crystallinity of biological apatites can be estimated by the value of the 1020/1030 ratio intensity (1020 cm^{-1}, nonstoichiometric apatites containing HPO_4^{2-}, CO_3^{2-}, and vacancies; 1030 cm^{-1}, stoichiometric apatites) and the increase at 1145 cm^{-1} peak[41].
10. The increase of 1090 cm^{-1} band intensity as compared with 1100 cm^{-1} indicated that apatite is becoming increasingly mature[41].

Organic components:

1. Peaks at 855 and 871 cm^{-1} indicates C-C stretch of proline and hydroxyproline[37].
2. Bands assigned to vibrations at 920 cm^{-1} are linked with P-OH stretching and the ν(C-C) of hydroxylated proline[39].
3. Collagen (proline/hydroxyproline/C-C skeletal of collagen backbone), is indicated by bands at 937 cm^{-1} [5].

4. Phenylalanine (C-C aromatic ring) is represented by peaks at 1001 cm^{-1} [5].
5. Peaks at 1610-1620 cm^{-1} are assigned to tyrosine side chain vibration[38].
6. Peaks at 1637 cm^{-1} are assigned to amide I ($C_1O_1…H_2O$)[39].
7. Peaks at 1694 cm^{-1} are assigned to amide I ($C_3O_3…H_2O$)[39].
8. The organic to inorganic ratio of bone components was assessed from the band intensities of the organic amide I (1694 cm^{-1}) with the peaks of the inorganic phosphatic component at 960 cm^{-1} [42].

Results

Results from Raman analysis may be observed in several maps of phosphate (961 cm^{-1}), carbonate (1070 cm^{-1}) and amide I (1656 cm^{-1}) peak intensities presented in Fig. 1. Truncated image (930 to 980 cm^{-1}) of the average spectra Raman maps from the phosphate PO_4^{3-}, at 960 cm^{-1} (v_1 mode) is shown in Fig. 2. Color mapping from hierarchical cluster analysis (HCA), classical least squares (CLS) and principal component analysis (PCA) images, corresponding to trabecular bone, are shown in Figs. 3, 4 and 5, respectively. Main values (arbitrary units -a.u.-) of Raman cluster analysis of trabecular bone are in Table 1, as the Amide III (1246-1270 cm^{-1}, 406.06 a.u.), CH_2 (1450 cm^{-1}, 307.82 a.u.), Amide I (1655-1667 cm^{-1}, 36.81 a.u.) peak intensities or the Crystallinity ($FWHM_{phosphate}$, 19.40; and, $FWHM_{carbonate}$, 31.62). The values of biochemical content of the sample corresponding to trabecular bone from a femoral neck biopsy, concerning *v2* [431 cm^{-1} peak position] (689.37 a.u.), *v1* [959 cm^{-1}] (2781.78 a.u.), CO_3^{2-}*v3* [1072 cm^{-1}] (510.17 a.u.), C-C proline [855 cm^{-1}] (384.95 a.u.) and Phenylalanine [1001 cm^{-1}] (228.62 a.u.) are shown in Table 2, which reflects the mineral and organic components of trabecular bone after Single Point Raman analysis.

Discussion

Mineralisation has been defined as the peak height ratio of phosphate v_1 and CH_2 in the present study[23]. The peak height of phosphate (2472.61 cm^{-1}) and the mineral to matrix ratio RMC_p and MMR_p (11.81 and 8.03, respectively) (Table 1) in the present study, commonly, provide these values and concerned with the relative degree of mineralisation[43,44], amount of mineralisation[34] or bone mineral content.

Symmetric bending mode (v_2) PO_4^{3-}, at 431 and 446 cm^{-1} peak heights, are recommended to be considered. These two bands (698.37 cm^{-1} and 619.39 cm^{-1}, respectively) (Table 2) are present in sound and demineralized/hypo-calcified substrata. In a demineralized/hypo-calcified spectra, 431 cm^{-1} peak intensity is greater than 446 cm^{-1} peak[45]. Furthermore, peaks at 579 and 590 cm^{-1} (v_4 asymmetric bending mode PO_4^{3-}) (146.86 and 165.60, respectively) (Table 2) show high intensity in the demineralized spectrum but a weak intensity in the sound spectrum[14]. The mineral-to-matrix ratio was lower with the minimal breaking force[40]. Fracture cases tended to have a high mineral-to-matrix ratio and a high carbonate-to-amide I ratio. Peaks at 1023, 1043, 1052 and 1069 cm^{-1}, are also high in a demineralized spectrum[14]. In the present study, 118.52, 282.21, 244.67 and 466.47 counts a.u. were achieved (Table 2). The intensity ratio plot shows enhanced 579/959 (0.05), 1043/959 (0.10), and 1069/959 (0.19) (Table 2) at the demineralized lesion[14]. The microdamaged and fractured bone regions may be measured by 963 cm^{-1} and 965 cm^{-1} [23], which shall attain a high wavenumber. 2146.03 and 1613.23 counts a.u. were achieved in our study (Table 2). The fractured bone tissue underwent a great remodeling process and was undermineralised as a result[34]. Areas where active remodeling is occurring can be measured through the strong monohydrogen phosphate v_1

vibration (~1003 cm^{-1}), which attained 205 of intensity of our samples (Table 2). It is a good probe of mineral structure substitution, in junction with the phosphate v_1 vibration (~960 cm^{-1})[37] (Fig 1A). Complementarily, the peak at 954 cm^{-1}, representative of PO_4^{3-} v_1 symmetric vibration, which is considered a good marker for calcification of the extracellular matrix[5] may be assessed. In our study, 2518.51 counts a.u. were obtained (Table 2).

Different phosphate v_1 spectral components have been attributed to various mineral species that compose the substrate[15], and other substitution (HPO_4^{2-}, or even CO_3^{2-}, in place of an OH^- (A-type carbonate)[15]. Chemical substitutions create crystal disorder hindering the ability of biological apatites to carry out their tissue-specific functions[46]. It can be observed in Fig 2 that the shape of the PO_4^{-3} v_1 band is non-Gaussian of unresolved shoulder bands that corresponds to other phosphate environments. Thus, the center of gravity of PO_4^{-3} v_1 band may report information about different mineral environments presented via changes in intensity or position of these shoulder bands. Any changes in shoulder bands are overlooked if only the peak center is examined. The observed spectral shift was mainly due to a change in the spacing between the cations and anions of phosphate[40]. Even more, three different levels of phosphate intensities were appreciated at the HCA Raman images, corresponding to three distinct centroids (Fig 3A) that reflected differences in Raman spectral distribution and chemical composition in mineral components at both phosphate and carbonate peaks (Fig 3E). The main centroid (HCA_1) (Fig. 3E, red areas in Figs 3A and 3B), which represents 39% of the variance, slightly increased the intensity of all peaks.

Changes in the spectral region of carbonate content have been ascribed to either growth of a carbonate peak or changes in the phosphate peak in response to the presence of carbonate in the lattice[47]. The presence of a prominent carbonate band around 1070 cm^{-1} (Fig. 1B) in the Raman spectrum (Table 1) is significant, because it means that the phosphate positions, in the apatite lattice, are susceptible to ionic substitution[34]. Single point Raman spectra attained at 430 (v_2 mode) and at 451 shift bands obtained peak heights of 698.37 cm^{-1} and 591.70 cm^{-1}, respectively (Table 2). These bands were assigned to vibrations of carbonated calcium phosphate[15]. Their increase is commonly associated to a decrease in crystallinity. It has been previously reported that the incorporation of carbonate is expressed as augmentation of the relative mineral concentration and in the gradient of mineral content (carbonate/phosphate). It deforms the crystal structure[45,48], causing a decrease in crystallinity[20], as a result of the decrease of non-stoichiometric apatites containing HPO_4^{2-}, CO_3^{2-}, and vacancies; an increase of stoichiometric apatites at 1030 cm^{-1} is commonly associated[10]. Bone is primarily a nonstoichiometric carbonated hydroxyapatite lattice. Strong intensity peak at 1072 cm^{-1} indicated substantial amount of B-type carbonate substitution in the phosphate mineral[15,37]. In our study, 510.17 counts a.u. were assessed. Nevertheless, the CLS fitting analysis (Fig. 4) in junction with the HCA analysis (Fig 3) and PCA analysis (Fig 5) attained different centroids whose variance reflect the contribution of the carbonate content of the chemical composition of this trabecular bone sample.

The mechanical strength of bone is not only dependent on the amount of mineralisation, but also on the degree of mineral crystallinity[4]. The term crystallinity refers to the order of a solid where a highly crystalline material displays long range sequence among its component atoms, and amorphous material. A simple Gaussian curve is usually used to

fit the phosphate band to obtain the full-width half-maximal (FWHM). 19.40 and 31.62 values of FWHM*p* and FWHM*c*, respectively, were obtained in the present study (Table 1). The crystallinity of biological apatites can also be estimated by the value of the 1020/1030 ratio intensity (1020 cm^{-1}, nonstoichiometric apatites containing HPO_4^{2-}, CO_3^{2-}, and vacancies; 1030 cm^{-1}, stoichiometric apatites) (0.53 in the present research) and the increase at 1145 cm^{-1} peak[41] (39.89 counts, in the present work) (Table 2). Stoichiometric hydroxyapatite may also be found in phosphate v_1 vibration, found at 963 cm^{-1}, whose values are 2146.03 counts at present work. On the contrary, amorphous calcium phosphate[14] or amorphous-like apatite species[37] may be found at 950 cm^{-1} and 956 cm^{-1}. Their values were 1622.18 and 2717.74 counts a.u, respectively (Table 2).

High mineral crystallinity yields narrower phosphate bandwidths, which is mirrored by low carbonate substitution (*i.e*, reduced carbonate-to-phosphate ratios)[4], 0.18, in the present study (Table 1). When the obtained carbonate-to-phosphate ratio or carbonate substitution are low, it points out high maturity and crystallinity, and an increase atomic order associated with a decrease of amorphous calcium phosphate compounds[25,26]. Raman measurements of carbonate-to-phosphate (at 959 cm^{-1}) ratios can also provide valuable insights into the chemical composition of human bones because it varies with bone architecture, age, and mineral crystallinity[4].

Collagen and mineral contribute to the structural behavior of bone tissue, but the microstructural characterisation in the second part of this study focused on collagen, which acts as a mineralisation template. Thus, it has been well established that the time-dependent properties of bone tissue are more influenced by collagen components than by mineral components[49]. Broken or distorted collagen cross-links reflects permanent

changes to the matrix and is thought to be one of the last processes to occur before bone failure[40]. The high relative intensity peak corresponding to the pyridinium ring may be, in general, associated with a non-reducible crosslinking formation, demonstrating that the first remineralisation is intrafibrillar. In our study, the pyridinium peak attained 197.76 counts of intensity (Table 1). Non-enzymatic cross links (*e.g*, pentosidine) exists in skeletal collagen due to spontaneous interaction of collagen proteins and free sugars or via oxidation reaction[50]. 59.22 counts of AGEs-pentosidine were obtained in the present research (Table 1). Increased pentosidine is associated with brittleness and reduced work of fracture of bone tissue[43].

The collagen network predominantly contributes to bone toughness and strength, and has little effect on bone stiffness[1]. The ratio amide I/CH_2 indicates altered collagen quality[36]. The term "bone quality" refers to the ensemble of composition and architectural properties of bone tissue that together determine bone properties and its ability to perform the mechanical function. A poor collagen matrix quality (Ratio Amide I/CH_2) is observed when the organic components show a lack of conformation and organisation of collagen. When bone is demineralised, the three-dimensional network of the collagen fibers that serves as the backbone of bone is revealed. This collagen network is flexible and tough. Because this network is the basic scaffolding on which the mineral is deposited, it contributes significantly to the mechanical integrity of bone[51]. The ratio Amide I/CH_2 reduction also hindered the scaffolding[36]. Collagen scaffolding contributes to progressive mineral deposition. Ratio amide I/AGEs-Pentosidine was indicative of the glycation reaction *vs* collagen scaffolding[36]. In the present work, 0.62 counts of intensity were achieved (Table 1). Newly formed bone tissue has less mineral content than pre-existing older bone tissue. The active trabecular bone remodeling produces less mineralised new

bone tissue[49]. Newly formed bone tissue has a higher collagen portion but not a fully mature collagen phase[49]. In this way, the increase in intensity of the 1090 cm^{-1} band if compared with 1100 cm^{-1} intensity values indicated that apatite is becoming increasingly mature[41]. In the present research, this value was 1.32 (Table 2).

The yield and ultimate strengths of bone decreased with increasing collagen denaturation[1]. When the nature of collagen resulted favorable, the peaks intensities corresponding to A-III, CH_2, A-1 and ratio A-I/A-III are high, indicating that organic components are well organized[32] for promoting apatite nucleation[52]. In our study, these values were 406.06, 307.82, 36.81, and 0.09 counts, respectively (Table 1). The molecular orientation, i.e., α-helices (1340 cm^{-1}) attained 59.07 counts of intensity, in the present research (Table 1). α-helices intensity peak is related to crystallisation[26].

Proline and hydroxyproline represent about 10% of the total collagen, *i.e.* 2% of the bone[42]. They are essential aminoacid markers for the presence of collagen[53]. Raman bands corresponding to proline (855 cm^{-1}) and hydroxyproline (871 cm^{-1}) showed high intensity peaks in demineralised substrata (384.95 and 188.92 wavebands, in the present research) (Table 2). Peak at 920 cm^{-1}, assigned to P-OH stretching and the *v*(C-C) of hydroxylated proline attained values of 204.83 counts of intensity (Table 2). The prolyl-hydroxylase notably increases the structural stability of collagen, as the hydroxylation of the proline aminoacid is an important biochemical process for maintaining the connective tissue[39]. Collagen (proline/hydroxyproline/C-C skeletal of collagen backbone), indicated by bands at 937 cm^{-1} [5], achieved an intensity band of 585.51 counts (Table 2). Phenylalanine (C-C aromatic ring), represented by peaks at 1001 cm^{-1} [5], achieved 228.62 counts of intensity (Table 2).

Band peak at 1062 cm^{-1} obtained 379.26 intensity counts (Table 2). This signal corresponds to proteoglycans, which form a multifaceted scaffold system with attached amorphous macromolecules, possibly lipids and other proteolipids complexes, that provide support and facilitate formation of new mineral[53]. Peaks at 1448 cm^{-1} and 1656 cm^{-1}, corresponding to lipids and proteins[5], attained values of 350.51 and 28.26 intensity counts, respectively (Table 2). Proteoglycans and glycosaminoglycans (or shape modulus complexes-lipids and proteolipids) participate in biomineralisation via the action of the highly negatively charged glycosaminoglycan side chains in recruiting and stabilizing positively charged calcium ions, conducting a biological signaling role[53]. The amide I band is representative of the secondary structure of proteins. Peak at 1610-1620 cm^{-1} is attributed to the amide I feature of bone and hydrated gel-like collagen. The wavenumber of this feature (26.82) (Table 2) corresponds to the spectral peak that is assigned to the Y8a tyrosine side chain of solution-phase collagen[38]. From a clinical standpoint, recovery[32] correct organisation[54], and collagen quality[36] may be inferred. In general, amide I at 1637 cm^{-1} (C_1O_1…H_2O), 1662 cm^{-1} (C_2O_2…H_4N_4) and 1694 cm^{-1} (C3O3… H_2O)[41] follow a similar trend. Their values, at the present work, achieved 49.74, 42.41 and 27.32 intensity counts, respectively (Table 2). The organic to inorganic ratio of bone components, assessed from the band intensities of the organic amide I (1694 cm^{-1}) (Fig. 1C) with the peaks of the inorganic phosphate component at 960 cm^{-1} [42] was 0.01, in the present work (Table 2).

Although the present study has many strengths, including the measurement of the trabecular bone at molecular levels, it also has several weakness, and the results obtained in this study should be considered within the context of the limitations. It is important to

emphasise that the different methods, used in the present study, measure different chemical quantities. In that respect, it is reasonable that each chemical quantity has different kinds of uncertainties and error distributions, and these errors do not just originate from the applied method itself, *i.e,* they are not "methods artifacts" [18].

Conclusions

The presented analysis is a first step in quantifying microstructural variations in both mineral and collagen structure of trabecular bone tissue.

Raman spectral properties of collagen and mineral are altered in the damaged bone. The cluster analysis and the single point mapping technique are useful tools to understand the detailed mechanisms of those structural modifications, in order to assess degenerative bone diseases and to evaluate and develop successful therapies.

Further studies to investigate the compositional organisation and interaction between mineral and collagen are necessary to the total characterisation of the substrate.

Conflict of interest

The authors state that none of them has a conflict of interest that relates to the content discussed in this manuscript.

All authors disclose any financial and personal relationships with other people or organisations that could inappropriately influence their work.

Acknowledgements

Project MAT2017-85999-P supported by the Ministry of Economy and Competitiveness (MINECO) of Spanish Government and European Regional Development Fund (ERDF).

In addition, the authors would like to thank the technical support of MS Marta L. DeCalle and Ph.D. Inmaculada Cabello for manuscript edition.

References

1. Wang X, Bank RA, TeKoppele JM, Agrawal CM. The role of collagen in determining bone mechanical properties. *J Orthop Res* 2011;**19**: 1021–6.

2. Jiroušek O. Nanoindentation of human trabecular bone-tissue mechanical properties compared to standard engineering test methods, nanoindentation in materials science. Dr. Jiri Nemecek (Ed.), In *Tech* 2012;**11**: 259-84.

3. Liu Y, Yao X, Liu YW, Wang Y. A Fourier transform infrared spectroscopy analysis of carious dentin from transparent zone to normal zone. *Caries Res* 2014;**48**: 320–9.

4. Morris MD, Mandair GS. Raman assessment of bone quality. *Clin Orthop Relat Res* 2011;**469**: 2160–9.

5. Kunstar A, Leijten J, van Leuveren S, Hilderink J, Otto C, van Blitterswijk CA, et al. Recognizing different tissues in human fetal femur cartilage by label-free Raman microspectroscopy. *J Biomed Opt* 2012;**17**, 116012.

6. Milly H, Festy F, Watson TF, Thompson I, Banerjee A. Enamel white spot lesions can remineralise using bio-active glass and polyacrylic acid-modified bio-active glass powders. *J Dent* 2014;**42**: 158–66.

7. Wang C, Wang Y, Huffman NT, Cui C, Yao X, Midura S, et al. Confocal laser Raman microspectroscopy of biomineralisation foci in UMR 106 osteoblastic cultures reveals temporally synchronized protein changes preceding and accompanying mineral crystal deposition. *J Biol Chem* 2009;**284**: 7100–113.

8. Bonifacio A, Beleites C, Vittur F, Marsich E, Semeraro S, Paoletti S, et al. Chemical imaging of articular cartilage sections with Raman mapping, employing uni- and multi-variate methods for data analysis. *The Analyst* 2010;**135**: 3193–204.

9. Almahdy A, Downey FC, Sauro S, Cook RJ, Sherriff M, Richards D, et al. Microbiochemical analysis of carious dentine using Raman and fluorescence spectroscopy. *Caries Res* 2012;**46**: 432–40.

10. Toledano M, Aguilera FS, Cabello I, Osorio R. Remineralization of mechanical loaded resin-dentin interface: a transitional and synchronized multistep process. *Biomech Model Mechanobiol* 2014;**13**: 1289–302.

11. Kobrina Y, Turunen MJ, Saarakkala S, Jurvelin JS, Hauta-Kasari M, Isaksson H. Cluster analysis of infrared spectra of rabbit cortical bone samples during maturation and growth. *Analyst* 2010;**135**: 3147–55.

12. Schlücker S, Schaeberle MD, Huffman SW, Levin IW. Raman Microspectroscopy: A Comparison of Point, Line, and Wide-Field Imaging Methodologies. *Anal Chem* 2003;**75**: 4312–8.

13. Moreno-Flores S, Toca-Herrera JL. *Hybridizing surfaces probe microscopies. Toward a full description of the Meso- and Nanoworlds.* Boca Raton: CRC Press; 2013.

14. Ko AC-T, Choo-Smith L-P, Hewko M, Leonardi L, Sowa MG, Dong CCS, et al. Ex vivo detection and characterization of early dental caries by optical coherence tomography and Raman spectroscopy. *J Biomed Opt* 2005;**10**, 031118.

15. LeGeros RZ, Kijkowska R, Bautista C, LeGeros JP. Synergistic effects of magnesium and carbonate on properties of biological and synthetic apatites. *Connect Tissue Res* 1995;**33**: 203–9.

16. Saito T, Arsenault AL, Yamauchi M, Kuboki Y, Crenshaw MA. Mineral induction by immobilized phosphoproteins. *Bone* 1997;**21**: 305–11.

17. Pathak S, Vachhani SJ, Jepsen KJ, Goldman HM, Kalidindi SR. Assessment of lamellar level properties in mouse bone utilizing a novel spherical nanoindentation data analysis method. *J Mech Behav Biomed Mater* 2012;**13**: 102–17.

18. Isaksson H, Malkiewicz M, Nowak R, Helminen HJ, Jurvelin JS. Rabbit cortical bone tissue increases its elastic stiffness but becomes less viscoelastic with age. *Bone* 2010;**47**: 1030–8.

19. Balooch G, Yao W, Ager JW, Balooch M, Nalla RK, Porter AE, et al The aminobisphosphonate risedronate preserves localized mineral and material properties of bone in the presence of glucocorticoids. *Arthritis Rheum* 2007;**56**: 3726–37.

20. Lee ML, Li Y, Feng YP, Carter CW. Study of frequency dependence modulus of bulk amorphous alloys around the glass transition by dynamic mechanical analysis. *Intermetallics* 2002;**10**: 1061–4.

21. Vanna R, Ronchi P, Lenferink ATM, Tresoldi C, Morasso C, Mehn D, et al. Label-free imaging and identification of typical cells of acute myeloid leukaemia and myelodysplastic syndrome by Raman microspectroscopy. *The Analyst* 2015;**140**: 1054–64.

22. Draper ERC, Morris MD, Camacho NP, Matousek P, Towrie M, Parker AW, et al. Novel assessment of bone using time-resolved transcutaneous Raman spectroscopy. *J Bone Miner Res* 2005;**20**: 1968–72.

23. Yerramshetty JS, Lind C, Akkus O. The compositional and physicochemical homogeneity of male femoral cortex increases after the sixth decade. *Bone* 2006;**39:** 1236-43.

24. McCreadie BR, Morris MD, Chen T-C, Sudhaker Rao D, Finney WF, Widjaja E, et al. Bone tissue compositional differences in women with and without osteoporotic fracture. *Bone* 2006;**39**: 1190–5.

25. Schwartz AG, Pasteris JD, Genin GM, Daulton TL, Thomopoulos S. Mineral distributions at the developing tendon enthesis. *PloS One* 2012;**7**: e48630.

26. Karan K, Yao X, Xu C, Wang Y. Chemical profile of the dentin substrate in non-carious cervical lesions. *Dent Mater* 2009;**25**: 1205–12.

27. Xu C, Wang Y. Cross-linked demineralized dentin maintains its mechanical stability when challenged by bacterial collagenase. *J Biomed Mater Res B Appl Biomater* 2011;**96**: 242–8.

28. Daood U, Iqbal K, Nitisusanta LI, Fawzy AS. Effect of chitosan/riboflavin modification on resin/dentin interface: spectroscopic and microscopic investigations. *J Biomed Mater Res A* 2013;**101**: 1846–56.

29. Jastrzebska M, Wrzalik R, Kocot A, Zalewska-Rejdak J, Cwalina B. Raman spectroscopic study of glutaraldehyde-stabilized collagen and pericardium tissue. *J Biomater Sci Polym* 2013;**14**: 185–97.

30. Sell DR, Monnier VM. Structure elucidation of a senescence cross-link from human extracellular matrix. Implication of pentoses in the aging process. *J Biol Chem* 1989;**264**: 21597–602.

31. Ager JW, Nalla RK, Breeden KL, Ritchie RO. Deep-ultraviolet Raman spectroscopy study of the effect of aging on human cortical bone. *J Biomed Opt* 2005;**10**: 034012.

32. Xu C, Wang Y. Chemical composition and structure of peritubular and intertubular human dentine revisited. *Arch Oral Biol* 2012;**57**: 383–91.

33. Carden A, Rajachar RM, Morris MD, Kohn DH. Ultrastructural changes accompanying the mechanical deformation of bone tissue: a Raman imaging study. *Calcif Tissue Int* 2003;**72**: 166–75.

34. Morris MD, Mandair GS. Raman assessment of bone quality. *Clin Orthop Relat Res* 2011;**469**: 2160–9.

35. McCreadie BR, Morris MD, Chen T-C, Sudhaker RD, Finney WF, Widjaja E, et al. Bone tissue compositional differences in women with and without osteoporotic fracture. *Bone* 2006;**39**: 1190–5.

36. Salehi H, Terrer E, Panayotov I, Levallois B, Jacquot B, Tassery H, et al. Functional mapping of human sound and carious enamel and dentin with Raman spectroscopy. *J Biophotonics* 2013;**6**: 765–74.

37. Timlin JA, Carden A, Morris MD, Rajachar RM, Kohn DH. Raman spectroscopic imaging markers for fatigue-related microdamage in bovine bone. *Anal Chem* 2000;**72**: 2229–36.

38. Ramakrishnaiah R, Rehman G, Basavarajappa S, Al Khuraif AA, Durgesh BH, Khan AS, et al. Applications of Raman Spectroscopy in dentistry: analysis of tooth structure. *Appl Spectrosc Rev* 2015;**50**: 332–50.

39. Garcia-Guinea JC, Jorge AC, Tormo L, Furio M, Crespo-Feo E, Correcher V, et al. Ossification vesicles with calcium phosphate in the eyes of the insect Copium teucrii (Hemiptera: Tingidae). *Scientific World J* 2011;**11**: 186–98.

40. Dooley KA, McCormack J, Fyhrie DP, Morris MD. Stress mapping of undamaged, strained, and failed regions of bone using Raman spectroscopy. *J Biomed Opt* 2009;**14**: 044018.

41. Magne D, Weiss P, Bouler J-M, Laboux O, Daculsi G. Study of the maturation of the organic (type i collagen) and mineral (nonstoichiometric apatite) constituents of a calcified tissue (dentin) as a function of location: a fourier transform infrared microspectroscopic investigation. *J Bone Miner Res* 2001;**16**: 750–7.

42. Kirchner MT, Edwards HGM, Lucy D, Pollard AM. Ancient and modern specimens of human teeth: a fourier transform Raman Spectroscopic study. *J Raman Spectrosc* 1997;**28**: 171–8.

43. Allen MR, Iwata K, Sato M, Burr DB. Raloxifene enhances vertebral mechanical properties independent of bone density. *Bone* 2006;**39**: 1130–5.

44. Polly BJ, Yuya PA, Akhter MP, Recker RR, Turner JA. Intrinsic material properties of trabecular bone by nanoindentation testing of biopsies taken from healthy women before and after menopause. *Calcif Tissue Int* 2012;**90**: 286–93.

45. Boyde A, Elliott JC, Jones SJ. Stereology and histogram analysis of backscattered electron images: age changes in bone. *Bone* 1993;**14**: 205–10.

46. Balooch G, Marshall GW, Marshall SJ, Warren OL, Asif SA, Balooch M., Evaluation of a new modulus mapping technique to investigate microstructural features of human teeth. *J Biomech* 2004;**37**: 1223–32.

47. Awonusi A, Morris MD, Tecklenburg MMJ. Carbonate Assignment and Calibration in the Raman Spectrum of Apatite. *Calcif Tissue Int* 2007;**81**: 46–52.

48. Zurick KM, Qin C, Bernards MT. Mineralization induction effects of osteopontin, bone sialoprotein, and dentin phosphoprotein on a biomimetic collagen substrate. *J Biomed Mater Res A* 2013;**101**: 1571–81.

49. Kim D-G, Jeong Y-H, Kosel E, Agnew AM, McComb DW, Bodnyk K, et al. Regional variation of bone tissue properties at the human mandibular condyle. *Bone* 2015;**77**: 98–106.

50. Allen MR, Gineyts E, Leeming DJ, Burr DB, Delmas PD. Bisphosphonates alter trabecular bone collagen cross-linking and isomerization in beagle dog vertebra. *Osteoporos Int USA* 2008;**19**: 329–37.

51. Yamashita J, Furman BR, Rawls HR, Wang X, Agrawal CM. The use of dynamic mechanical analysis to assess the viscoelastic properties of human cortical bone. *J Biomed Mater Res* 2001;**58**: 47–53.

52. Toledano M, Cabello I, Vílchez MAC, Fernández MA, Osorio R. Surface microanalysis and chemical imaging of early dentin remineralization. *Microsc Microanal* 2014;**20**: 245–56.

53. Bertassoni LE, Stankoska K, Swain MV. Insights into the structure and composition of the peritubular dentin organic matrix and the lamina limitans. *Micron* 2012;**43**: 229–36.

54. Toledano M, Aguilera FS, Sauro S, Cabello I, Osorio E, Osorio R. Load cycling enhances bioactivity at the resin-dentin interface. *Dent Mater* 2014;**30**: e169-88.

Table 1. Main values (a.u.) of Raman cluster analysis of trabecular bone.

MINERALS				ORGANICS		
Bone Mineral Content (BMC)	Phosphate [960]	Peak	2472.61	**Crosslinking**	Pyridinium [1032]	197.76
		Area	66523.7		AGEs-Pentosidine [1550]	59.22
		RMC_P	11.81	**Nature and secondary structure of collagen**	A-III [1246-1270]	406.06
		MMR_P	8.03		CH_2 [1450]	307.82
	Carbonate [1070]	Peak	459.64		A-I [1655-1667]	36.81
		Area	18970.7		Ratio A-I/A-III	0.09
		RMC_C	2.19		Ratio A-I/AGEs-pentosidines	0.62
		MMR_C	1.50		Ratio A-I/CH_2	0.12
Crystallinity (FWHM)		Phosphate $FWHM_P$	19.40		α-helices [1340]	59.07
		Carbonate $FWHM_C$	31.62			
GMC Ratio C/P			0.18			

Abbreviations: RMC: Relative Mineral Concentration between mineral/Phenyl (1003 cm^{-1}); MMR: Mineral (Phosphate) /Matrix (CH2) Ratio; FWHM: Full-width half-maximum; GMC: Gradient in Mineral Content; A: amide; AGEs: advanced glycation end products.
The peaks values have been normalised to the basis intensity of the symmetric phosphate band, near 960 cm^{-1}. Peaks positions are expressed in cm^{-1}.

Table 2. Mineral and organic components (a.u.) of trabecular bone after Single Point Raman analysis.

MINERALS				ORGANICS	
v2 [430-431]	698.37	*v1* [1003]	204.89	C-C proline [855]	384.95
v2 [446]	619.39	PO_4^{3-}*v3* [1023]	118.52	C-C hydroxyproline [871]	188.92
v2 [451]	591.70	PO_4^{3-}*v3* [1043]	282.21	C-C hydroxylated proline [920]	204.83
FA [575]	130.95	PO_4^{3-}*v3* [1052]	244.67	Collagen [937]	585.51
PO_4^{3-}*v4* [579]	146.86	CO_3^{2-}*v3* [1069]	466.47	Phenylalanine [1001]	228.62
PO_4^{3-}*v4* [590]	165.60	CO_3^{2-}*v3* [1072]	510.17	Proteoglycans [1062]	379.26
v1 [950]	1622.18	[1145]	39.89	Lipids and proteins- CH_2[1448]	350.51
v1 [954]	2518.51	R *579/959*	0.05	Lipids and proteins- AI [1656]	28.26
v1 [956]	2717.74	R *1043/959*	0.10	Tyrosine [1610-20]	26.82
v1 [959]	2781.78	R *1069/959*	0.17	Amide I [1637]	49.74
v1 [960]	2657.44	R *1020/1030*	0.53	Amide I [1662]	42.41
v1 [963]	2146.03	R *1090/1100*	1.32	Amide I [1694]	27.32
[965]	1613.23			R Amide I [1694]/960	0.01

Abbreviations: FA: Fluoridated Apatite; R: Ratio.
The peaks values have been normalised to the basis intensity of the symmetric phosphate band, near 960 cm^{-1}. Peaks positions between brackets are expressed in cm^{-1}.

Figure Legends

Figure 1: Raman analysis of trabecular bone. A: 2D micro-Raman map of the phosphate peak (961 cm^{-1}) intensities. B: 2D micro-Raman map of the carbonate peak (1070 cm^{-1}) intensities. C: 2D micro-Raman map of the amide I peak (1656 cm^{-1}) intensities. At this map, blue represents the lowest peak intensity, while the red represents the highest.

Figure 2: Truncated image (930 to 980 cm^{-1}) of the average spectra Raman maps (red bold line) from the phosphate PO_4^{3-}, at 960 cm^{-1} (v_1 mode). The observed line-coloured are the Gaussian–Lorentzian profile shapes for each band. The shape of the PO_4^{-3} v_1 band is Gaussian–Lorentzian of unresolved shoulder bands that corresponds to other phosphate environments. The center of gravity of PO_4^{-3} v_1 band is a useful way to gather information about different mineral environments present *via* changes in intensity or position of these shoulder bands.

Figure 3: Colour mapping from hierarchical cluster analysis **(**HCA) images corresponding to trabecular bone. Three levels of HCA clustering images are shown and grouped into *k* clusters (*k*=3), each cluster corresponding to a set of Raman shift. Areas of distinct colours have differences in Raman spectral distribution and chemical composition. Each centroid cluster is assigned to a different colour [(red (B), green (C) and blue (D)], thus obtaining a false colour-image of the substrate on the basis of similar spectral features. A: a merged image from the three centroid clusters B, C and D. Upon attributing different colours to each centroid image and setting the colour scale so that intensely coloured region (*i.e.*, pixels having high intensity values) are enhanced over "white" regions (*i.e.*, pixels having medium-low relative intensity values), these can be merged into a single image depicting the spatial distribution of different chemical species,

each colour corresponding to the set of Raman shifts characterizing that chemical species. Units on the colour scale bar are arbitrary units of integrated normalised intensity. E: average Raman spectra of the trabecular bone, showing the assignments for bone mineral and matrix-specific Raman bands, in the region from 400 to 1700 cm^{-1}.

Figure 4: Colour mapping from classical least squares (CLS) fitting analysis corresponding to trabecular bone. Three levels of CLS clustering images are shown and grouped into *k* clusters (*k*=3), each cluster corresponding to a set of Raman shift which reflects position, width, amplitude and area. Areas of distinct colours have differences in Raman spectral characteristics. Each centroid cluster is assigned to a different colour [(red (B), green (C) and blue (D)], thus obtaining a false colour-image of the substrate on the basis of similar spectral features. The excitation emission map spectra correction methods facilitate resolution of the exact spectral components in structure, despite their highly overlapping absorbance and emission spectra. A: merged image from the three centroid clusters B, C and D. E: an average Raman spectra of the trabecular bone, showing the assignments for bone mineral and matrix-specific Raman bands, in the region from 400 to 1700 cm^{-1}.

Figure 5: Colour mapping from principal component analysis (PCA) images corresponding to trabecular bone. Three levels of PCA clustering images are shown and grouped into *k* clusters (*k*=3), each cluster corresponding to a set of Raman shift. Areas of distinct colours have differences in Raman spectral distribution and chemical composition. Each centroid cluster is assigned to a different colour [(red (B), green (C) and blue (D)], thus obtaining a false colour-image of the substrate on the basis of similar spectral features. A: a merged image from the three centroid clusters B, C and D. Units

on the colour scale bar are arbitrary units of integrated normalised intensity. E: average Raman spectra of the trabecular bone, showing the assignments for bone mineral and matrix-specific Raman bands, in the region from 400 to 1700 cm^{-1}, but concerned to the red cluster whose variance was ~99%.

Figure 1

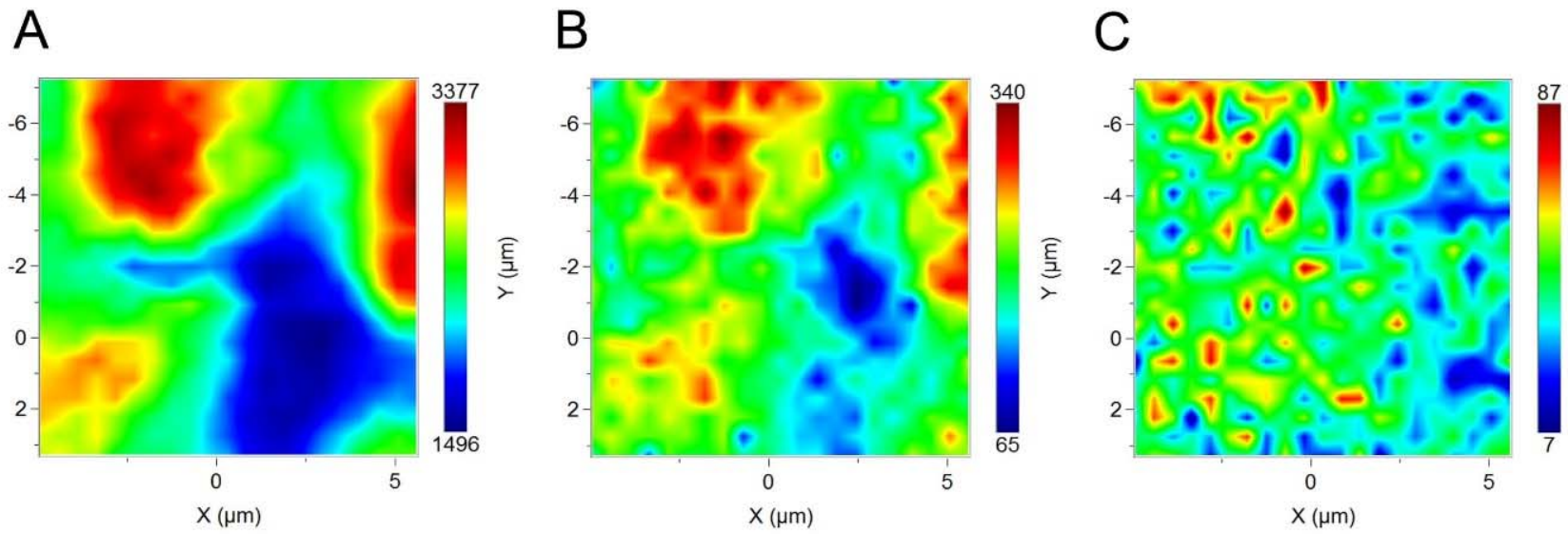

Figure 2

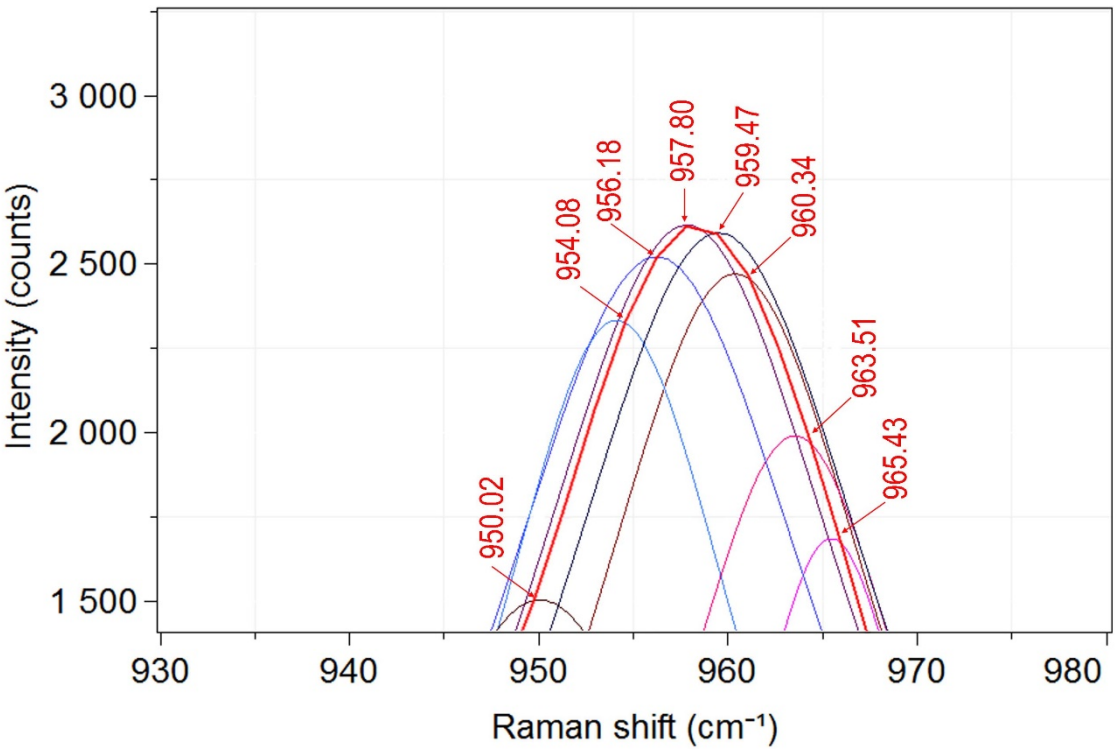
3 000
2 500
2 000
1 500
Intensity (counts)
930
940
950
960
970
980
Raman shift (cm⁻¹)
950.02
954.08
956.18
957.80
959.47
960.34
963.51
965.43

Figure 3

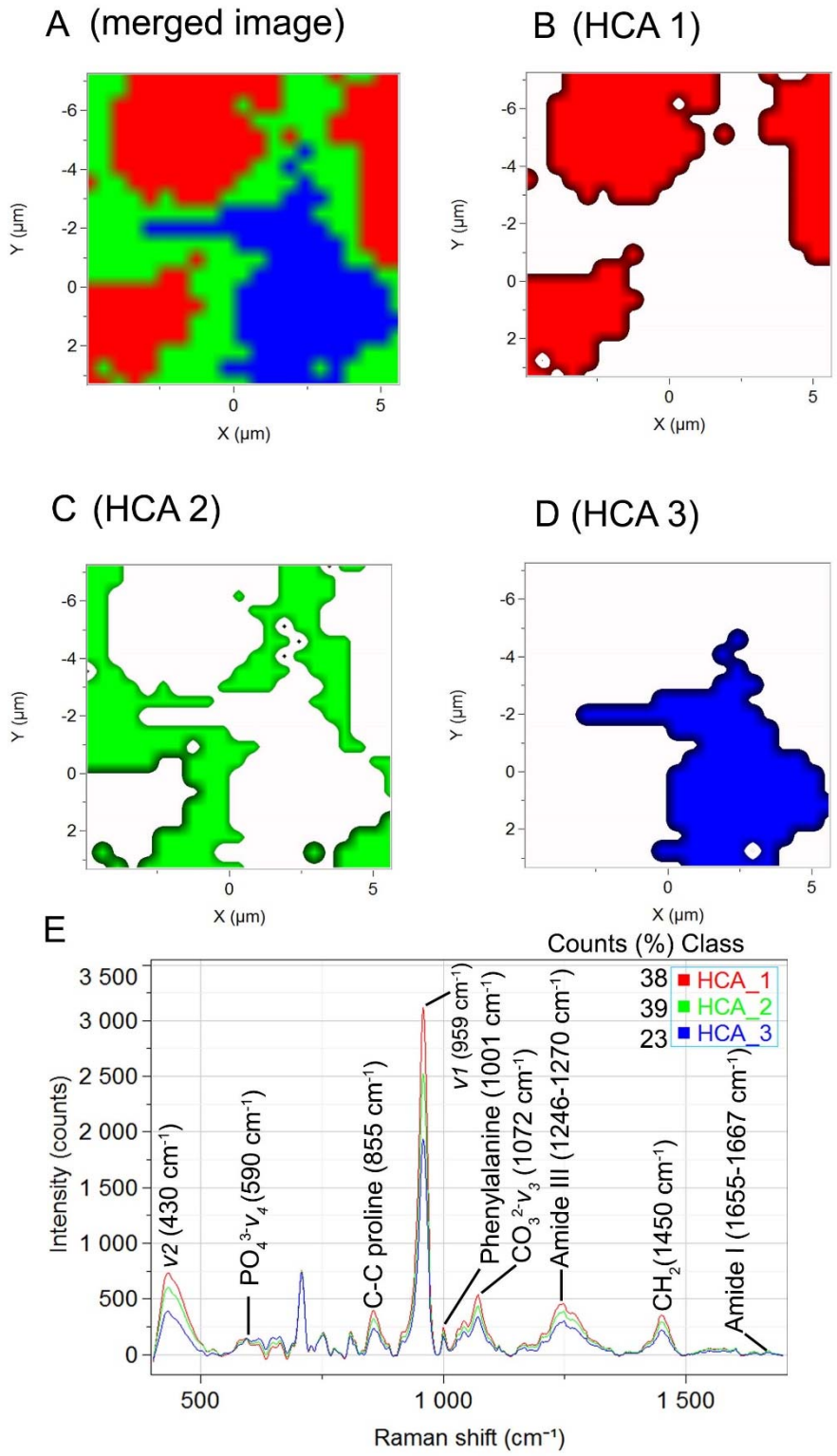
A (merged image)
B (HCA 1)
C (HCA 2)
D (HCA 3)
E
Y (µm)
X (µm)
Counts (%) Class
38 HCA_1
39 HCA_2
23 HCA_3
Intensity (counts)
Raman shift (cm⁻¹)
v2 (430 cm⁻¹)
PO4 3- v4 (590 cm⁻¹)
C-C proline (855 cm⁻¹)
v1 (959 cm⁻¹)
Phenylalanine (1001 cm⁻¹)
CO3 2- v3 (1072 cm⁻¹)
Amide III (1246-1270 cm⁻¹)
CH2 (1450 cm⁻¹)
Amide I (1655-1667 cm⁻¹)

Figure 4

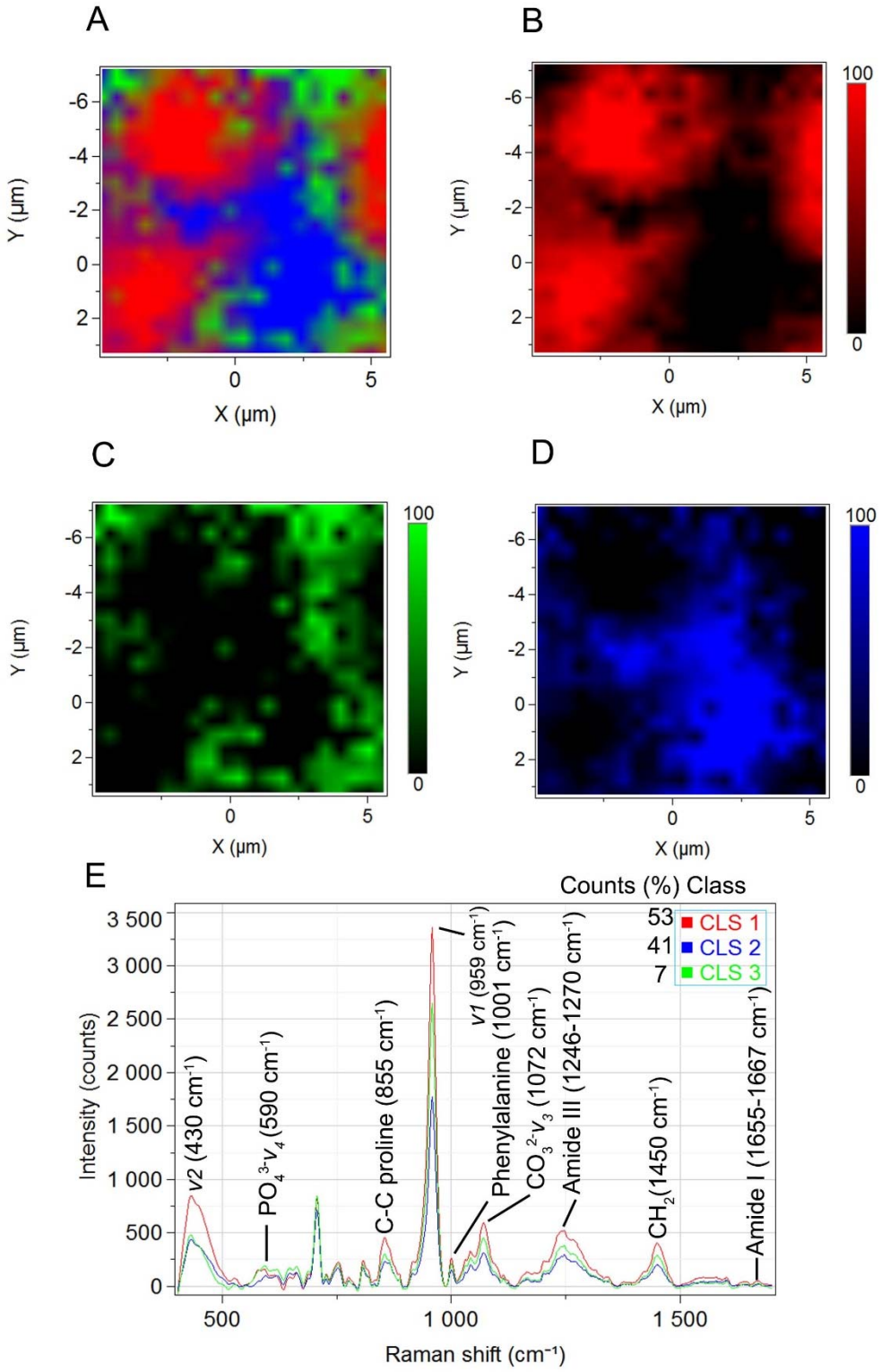
A
B
C
D
E
Y (µm)
X (µm)
100
0
Counts (%) Class
53 CLS 1
41 CLS 2
7 CLS 3
Intensity (counts)
Raman shift (cm⁻¹)
ν2 (430 cm⁻¹)
PO4 3- ν4 (590 cm⁻¹)
C-C proline (855 cm⁻¹)
ν1 (959 cm⁻¹)
Phenylalanine (1001 cm⁻¹)
CO3 2- ν3 (1072 cm⁻¹)
Amide III (1246-1270 cm⁻¹)
CH2 (1450 cm⁻¹)
Amide I (1655-1667 cm⁻¹)

Figure 5

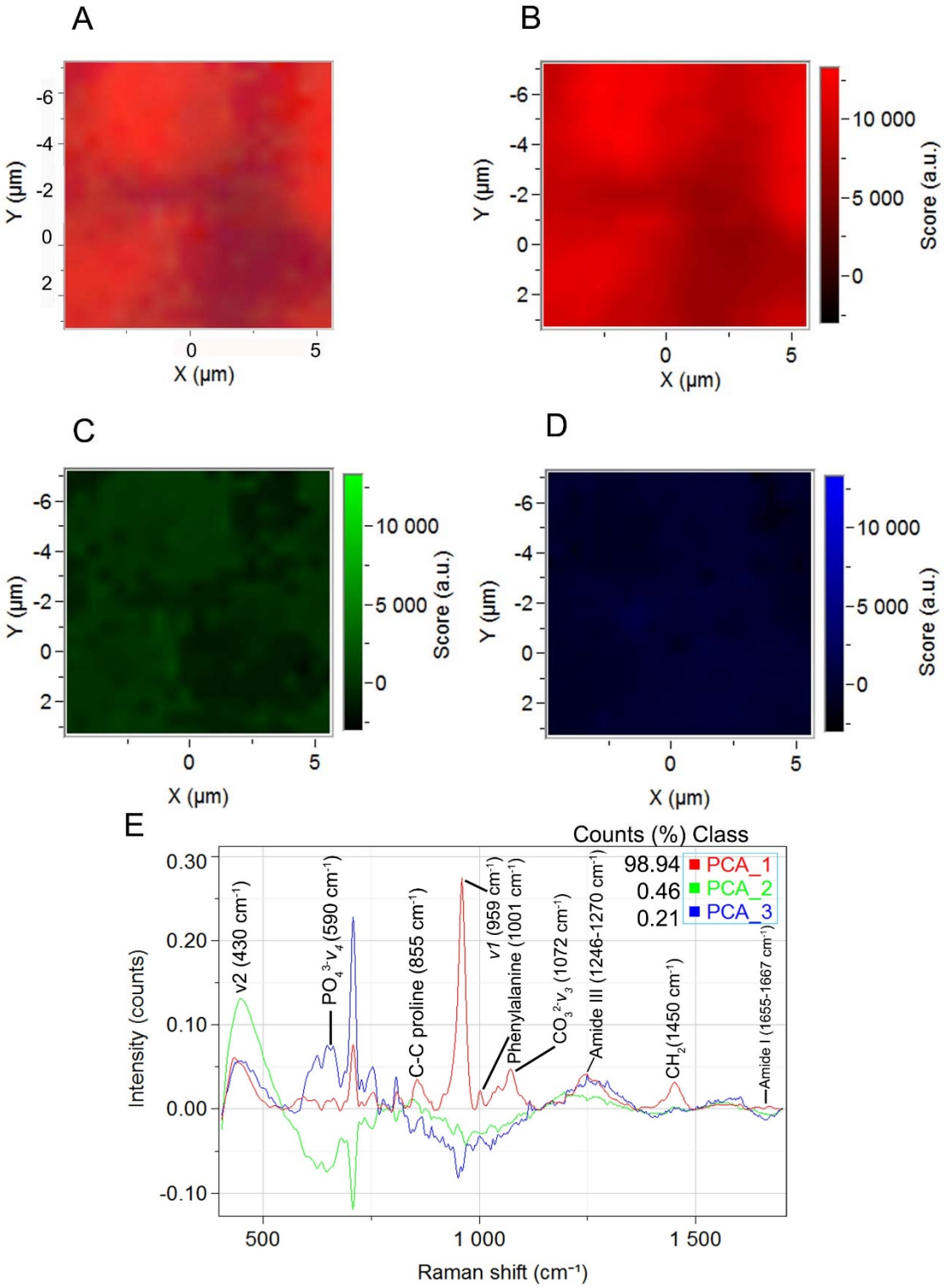
A
B
C
D
E
Y (µm)
X (µm)
Score (a.u.)
10 000
5 000
0
Counts (%) Class
98.94 PCA_1
0.46 PCA_2
0.21 PCA_3
Intensity (counts)
Raman shift (cm⁻¹)
v2 (430 cm⁻¹)
PO4 3-v4 (590 cm⁻¹)
C-C proline (855 cm⁻¹)
v1 (959 cm⁻¹)
Phenylalanine (1001 cm⁻¹)
CO3 2-v3 (1072 cm⁻¹)
Amide III (1246-1270 cm⁻¹)
CH2 (1450 cm⁻¹)
Amide I (1655-1667 cm⁻¹)